

Dynamical renormalisation of a spin Hamiltonian via high-order nonlinear magnonics

C. Schoenfeld, L. Feuerer, D. Wuhler, W. Belzig, A. Leitenstorfer, and D. Bossini^{†*}

*Department of Physics and Center for Applied Photonics,
University of Konstanz, D-78457 Konstanz, Germany*

D. Juraschek

School of Physics and Astronomy, Tel Aviv University, Tel Aviv 6997801, Israel

(Dated: October 31, 2023)

arXiv:2310.19667v1 [cond-mat.str-el] 30 Oct 2023

The macroscopic magnetic order in the ground state of solids is determined by the spin-dependent Hamiltonian of the system. In the absence of external magnetic fields, this Hamiltonian contains the exchange interaction, which is of electrostatic origin, and the spin-orbit coupling, whose magnitude depends on the atomic charge¹. Spin-wave theory provides a representation of the entire spectrum of collective magnetic excitations, called magnons, assuming the interactions to be constant and the number of magnons in the system negligible^{1,2}. However, the electric field component of light is able to perturb electrostatic interactions, charge distributions and, at the same time, can create a magnon population. A fundamental open question therefore concerns the possibility to optically renormalise the spin Hamiltonian. Here, we test this hypothesis by using femtosecond laser pulses to resonantly pump electric-dipole-active pairs of high-energy magnons near the edges of the Brillouin zone³⁻⁵. The transient spin dynamics reveals the activation and a surprising amplification of coherent low-energy zone-centre magnons, which are not directly driven. Strikingly, the spectrum of these low-energy magnons differs from the one observed in thermal equilibrium, the latter being consistent with spin-wave theory. The light-spin interaction thus results in a room-temperature renormalisation of the magnetic Hamiltonian, with an estimated modification of the magnetic interactions by 10% of their ground-state values. We rationalise the observation in terms of a novel resonant scattering mechanism, in which zone-edge magnons couple nonlinearly to the zone-centre modes. In a quantum mechanical model, we analytically derive the corrections to the spectrum due to the photo-induced magnon population, which are consistent with our experiments. Our results present a milestone on the path towards an all-optical engineering of Hamiltonians in solids. The established mechanisms to generate coherent collective excitation of spins, i.e. coherent magnons, via laser pulses can be grouped into two classes: non-resonant and resonant. The first class is based on an impulsive form of inelastic light scattering, namely impulsive stimulated Raman scattering (ISRS), and is phenomenologically described in terms of opto-magnetic effects that produce effective magnetic fields^{6,7}, such as the inverse Faraday⁸ or inverse Cotton-Mouton effects⁹. This approach relies on visible or near-infrared laser pulses, typically tuned to the transparency region of the material in order to limit energy dissipation⁷. Under such conditions, numerous successful demonstrations of excitation and manipulation of coherent magnons both at the centre (low-energy) and near the edges (high-energy) of the

* davide.bossini@uni-konstanz.de

Brillouin zone have been implemented^{8–10}. In the second class, magnons at the zone-centre have been photo-induced by employing a variety of resonant mechanisms such as magnetic dipole transitions^{11,12}, orbital transitions^{13,14}, exciton-magnon processes^{15–17} and the optical generation of lattice modes^{18–20}. A spin-conserving electric-dipole process, directly linked to the exchange interaction^{3–5}, enables the optical resonant drive of zone-edge magnon pairs. This link is the gateway to resonantly perturb the exchange interaction and, in doing so according to theoretical predictions^{21,22}, to modify the spectrum of magnons via an intrinsically nonthermodynamical magnetic excited state. In fact, the value of temperature required for a massive thermal population of zone-edge magnons typically exceeds the ordering temperature²³. Therefore, a massive population of magnon pairs near the zone edges, named *two-magnon* (2M) mode, can be induced exclusively optically, as indicated by means of ground-state spectroscopic techniques in the mid-infrared range^{24,25}. However, despite the intriguing and exotic theoretical predictions aforementioned^{21,22}, no experiment has to date addressed the fundamental scientific question: Which spin dynamics can be induced by resonantly and selectively exciting the 2M mode?

In order to tackle this question, we study the case of a single crystal of hematite (α -Fe₂O₃, see Methods). At room temperature, the two antiferromagnetically coupled sublattices of Fe in α -Fe₂O₃ are slightly canted due to the Dzyaloshinski-Moriya interaction (DMI), which weakly competes with the Heisenberg exchange^{25–27} allowing a small magnetization in the plane of the sample (see Fig. 1(a)). The spin Hamiltonian of α -Fe₂O₃ can be written as^{2,28}

$$\hat{H} = J \sum_{i,j} \hat{s}_i^\uparrow \cdot \hat{s}_j^\downarrow - 2\mu_0 H_a \sum_i \hat{S}_{iz}^\uparrow + 2\mu_0 H_a \sum_i \hat{S}_{iz}^\downarrow + \sum_{i,j} \mathbf{D}_{ij} \cdot \hat{s}_i^\uparrow \times \hat{s}_j^\downarrow, \quad (1)$$

where $(\hat{s}_i^\uparrow, \hat{s}_i^\downarrow)$ represent the (unit) vectors corresponding to spins of the two sublattices (Fig. 1(a)), J is the Heisenberg exchange interaction, H_a is the anisotropy effective field and \mathbf{D}_{ij} represents the DMI. Notice that also the exchange and the DMI can be expressed in terms of the effective fields H_e and H_D , via the relationships $J = 2\mu_0 H_e M_0$ and $D = 2\mu_0 H_D M_0$ ²⁸. Here M_0 is the saturation magnetisation of both sublattices and $\mu_0 = (g/2)\mu_B$, with g and μ_B representing the electronic g-factor and the Bohr magneton, respectively.

We show the absorption spectrum of α -Fe₂O₃ in the mid-infrared spectral range in Fig. 1(b). A peak centred around 45 THz is identified as the 2M Mode²⁵. The established exchange mechanism allowing to generate magnon pairs by means of the electric field component of light^{3–5}

is sketched in Fig. 1(c) and discussed in the Methods section. Our experimental approach (Fig. 1(a)) relies on the tunability of the photon energy and polarisation of our excitation beam in the 37-53 THz range, which allows us to quantitatively assess the effect of the resonant and off-resonant pumping of the 2M mode on the spin dynamics. The transient magneto-optical response of α -Fe₂O₃ is detected by monitoring the changes of the ellipticity of the polarisation²⁸ of 20-femtosecond-long probe pulses, with a central photon energy in the near-infrared range, i.e. ≈ 1 eV (details in Methods).

First, we excite the material off-resonantly, tuning the central frequency of the pump beam to 37 THz. The results are shown as a yellow trace in Fig. 2(a). The spin dynamics displays two oscillatory components with frequencies of 165 GHz and 20 GHz, as displayed in the Fourier transform of the data (Fig. 2(b)). These values are in good agreement with the eigenfrequencies of the quasi-antiferromagnetic (q-AFM) and quasi-ferromagnetic (q-FM) resonances, which are low-energy magnon modes at the centre of the Brillouin zone²⁸⁻³⁰. This assignment of the harmonic contributions to the signal is further corroborated by the dependences of the magnon frequencies on the externally applied magnetic field, qualitatively and quantitatively consistent with the expected trends for the q-AFM and q-FM modes^{27,29} (Fig. 2(c)).

Second, we tune the central frequency of the pump beam to 45 THz to unravel the dynamical response of the magnetic system to the resonant drive of the 2M Mode. The green time trace in Fig. 2(a) reveals that the amplitudes of both modes are vigorously enhanced and the respective frequencies are modified as well (see Fig. 2(b)). This striking evidence calls for a systematic investigation of the dependence of the spin dynamics on the pump central frequency. From the dataset shown in Extended Data Fig. 2, we extract the amplitude of both the q-AFM and q-FM modes by fitting each time trace (see Methods). The trends of the amplitudes are plotted in Fig. 3(a) and they show that both modes are strongly amplified ($\times 5$ for the q-AFM mode and $\times 3.5$ for the q-FM mode) by pumping α -Fe₂O₃ in resonance with the 2M Mode. The fitting procedure provides also the eigenfrequencies of the two modes, whose spectral dependence is shown in Fig. 3(b). The results display a relative modification of the frequency for both modes amounting to approximately 4% of the original values. In particular, the frequency of the lower-energy q-FM mode redshifts, while the higher-energy q-AFM mode is blueshifted. Remarkably, the coupling to the intense mid-infrared light pulses induces quantitatively the same energy splitting obtained in α -Fe₂O₃ by applying a strong magnetic field (>5 T), which results in coupling the two low-energy magnon modes²⁶. We emphasise that the q-AFM and

q-FM modes are not resonantly driven, as their eigenfrequencies (165 GHz and 20 GHz) are orders of magnitude lower than the spectral content of our mid-infrared laser pulses, as shown in Extended Data Fig. 1. We do resonantly drive pairs of zone-edge magnons, which results in the excitation and a sizeable modification of the spectrum of both zone-centre modes.

Several manifestations of coherent magnonics on fundamental timescales have been reported so far, such as frequency mixing of ground-state frequencies^{16,31–34} or change of frequencies observed by driving the system across magnetic critical points (i.e. phase transitions)^{13,20}. All these observations describe physics at the centre of the Brillouin zone and are fully consistent with the dispersion relation calculated in terms of the canonical spin-wave theory. Here, the resonantly pumped zone-edge magnons couple to zone-centre magnons, whose spectra are consequently modified. We highlight that this tantalizing phenomenon is unprecedented not only for magnetic systems. In fact, the coherent coupling between zone-edge and zone-centre quasiparticles on fundamental timescales, concomitant with the modification of the spectrum, is simply unheard of for any type of quasiparticles in solids (phonons, plasmons, polaritons, etc.). Our results thus establish a landmark concept for condensed-matter physics in general. The experimental evidence cannot be interpreted in terms of conventional spin-wave theory. To quantify the photoinduced perturbation of the magnetic system in our experiment, we recall that the eigenfrequencies of the q-AFM and q-FM modes are defined by the effective fields due to the DMI (H_D) and by H_c^2 , which is the product of the exchange and anisotropy fields defined previously^{27,28} (see Eqs. (11) and (12) in Methods). Describing the changes of the eigenfrequencies in Fig. 3(b) in terms of modifications of the effective fields results in $\Delta H_D/H_D \approx -9\%$ and $\Delta H_c^2/H_c^2 \approx 12\%$ (see Methods). Therefore, our pumping strategy realises a dynamical effective renormalisation of the magnetic Hamiltonian given in Eq. (1).

Third, we investigate the excitation mechanism at play both for off- and on-resonance conditions. We measure the dependence of the spin dynamics on the polarisation of the excitation beam, pumping both far-away-from and resonantly with the 2M Mode, as visualised in Fig. 1(b). By fitting all the time traces displayed in Extended Data Fig. 3 we retrieve the amplitudes of the q-FM and q-AFM modes. Figure 4(a) shows that the amplitude of the q-FM mode has a periodic dependence on the polarisation of the pump beam, as typically observed for ISRS-induced magnons^{6,8,9}. Under both off- and on-resonance driving conditions, we find the same periodicity of 180° . Similar results are obtained for the q-AFM mode (Fig. 4(b)). The experiments demonstrate that tuning the central frequency of the pump beam to be resonant

with the 2M mode enhances the amplitude of the zone-centre magnons and modifies their frequencies, but does not affect the symmetry of the photoexcitation. This result points decisively towards the existence of a single excitation mechanism on a microscopic level, which we activate either off-resonantly or resonantly. In order to ascertain the nature of this mechanism, we perform additional experiments. Hence we measure the absorption of the mid-infrared pump beam with frequencies of 45 THz (resonant with the 2M Mode) and 40 THz (off-resonant) as a function of its polarisation. The results shown in Fig. 4(c) demonstrate that the absorption is isotropic in the ab -plane of α -Fe₂O₃ for both frequencies of the mid-infrared beam. On the other hand, the coherent spin dynamics for both modes is not isotropic in the plane. It follows then that the absorption of light cannot be the origin of the generation and amplification of the coherent magnons, thus ruling out thermal mechanisms. We further characterise both the on-resonance and off-resonance excitation regime by measuring the fluence dependence of the zone-centre collective spin excitations (Extended Data Fig. 4). The amplitudes of the low-energy magnon modes scale linearly with the fluence in all data sets. This scaling together with the polarisation dependence (Fig. 4(a-b)) are consistent with light-scattering mechanisms⁶⁻⁸. As ISRS is the topical non-thermal excitation mechanism of coherent magnons, we extend its canonical formalism, which describes a non-resonant light-matter interaction regime, to the resonant case. Consequently, the enhancement of the amplitudes observed in Fig. 3(a) can be taken into account. While the general idea of resonant ISRS may appear straightforward, the novelty of the mechanism we introduce here, is that the resonance of the Raman-scattering cross section of zone-centre spin waves is provided by zone-edge magnons. Hence we name this novel mechanism two-magnon resonant Raman scattering (2MRRS). The spin dynamics triggered by the 2M excitation can be described in terms of a spin-correlation function, $C_{ij,\mathbf{k}} \sim \langle S_{i,\mathbf{k}} S_{j,-\mathbf{k}} \rangle$ ^{10,35}, where i, j indicate ionic sites and $\mathbf{k} = \pi/a$ in our case. Because the electric dipole moment of the 2M excitation is given by $p_{i,\mathbf{k}} = \Pi_{ijk,\mathbf{k}} S_{j,\mathbf{k}} S_{k,-\mathbf{k}}$ ³⁻⁵, we can write the interaction potential for the absorption process as

$$H_{\text{int}} = \Pi_{ijk,\pm\mathbf{k}} C_{ij,\pm\mathbf{k}} E_{\mathbf{k}}. \quad (2)$$

The resonantly driven 2M excitation then couples nonlinearly to the q-AFM and q-FM modes (see Fig. 5), which can be described in the macrospin approximation,

$$H_{\text{nonlinear}} = \kappa_{ijk,\pm\mathbf{k}} C_{ij,\pm\mathbf{k}}^2 M_k + \kappa'_{ijkl,\pm\mathbf{k}} C_{ij,\pm\mathbf{k}}^2 L_k L_l, \quad (3)$$

where the first and second terms describe the couplings to the q-FM and q-AFM modes, respectively. These terms resemble the forms of the inverse Faraday^{6,8} and the inverse Cotton-Mouton^{9,36} effects, respectively, whose Raman-tensor components are resonantly enhanced by the 2M Mode. Measurements performed with circularly polarised pump pulses demonstrate that the q-FM mode follows the helicity dependence of the inverse Faraday effect, while the q-AFM mode shows a dependence on the linear polarization of light typical of the inverse Cotton-Mouton effect (Extended Data Fig. 5, 3 and Fig. 4)^{8,9,36}. The details of the model are provided in Methods. It is important to highlight that if the photon energy of the pump beam is tuned far away from the resonance, the terms provided in Eq. (3) become negligible and the conventional ISRS description^{6,8,9} is recovered.

We turn now the discussion to the frequency shifts of the low-energy magnons observed by resonantly pumping the zone-edge magnons (Fig. 3**(b)**). This effect can be confidently ascribed to the nature of the transition pumped, since possible contributions arising from single-mode anharmonicity in the spin dynamics are ruled out experimentally (see Extended Data Fig. 4). The shifts of the eigenfrequencies imply a modification of the interactions, which we have already estimated quantitatively. It follows that a comprehensive theoretical description of the observation should reproduce the photoinduced dynamics of all the magnetic interactions in α -Fe₂O₃, as a function of the laser parameters. With this starting point, the temporal evolution of the magnon spectra should be calculated. Developing such a daunting theory is well beyond the scope of the current manuscripts. Nevertheless, we formulate a model that aims at deriving some corrections to the predictions of the canonical spin-wave theory. In particular, the renormalisation of the exchange in a ferromagnet induced by the thermal population of magnons has been derived in the literature². Inspired by the work of Kittel², we consider the case of a photoinduced population of zone-edge magnons in a weak ferromagnet. Although the time-dependences of the interactions and of the population are not explicitly taken into account, we derive the renormalisation of the exchange and, thus, of the magnetic eigenfrequencies. The model Hamiltonian that we employ (Eq. (21)) is minimal in comparison with the full Hamiltonian of α -Fe₂O₃³⁷. However, it is able to reproduce the ground state (via the fictitious field B_{DM} effectively canting the two sublattices) and still allows a fully analytical treatment of the problem. In particular, we derive the corrections to the frequencies of the q-FM and q-AFM

modes (see Methods). We obtain

$$\Delta\omega_{\text{q-FM}} \approx -\frac{n_{\frac{\pi}{2}}}{2SN\omega_{\text{q-FM},0}} \left(|B_{\text{DM}}|^2 - \frac{1}{4}S^2KJ_0 \right), \quad (4)$$

$$\Delta\omega_{\text{q-AFM}} \approx \frac{n_{\frac{\pi}{2}}}{2SN\omega_{\text{q-AFM},0}} \left(|B_{\text{DM}}|^2 - \frac{3}{4}S^2KJ_0 \right). \quad (5)$$

The unperturbed frequencies are represented by $\omega_{\text{q-FM},0}$ and $\omega_{\text{q-AFM},0}$, the factor $n_{\frac{\pi}{2}}$ is the photo-induced magnon population at the edges of the Brillouin zone, while N and S represent the number of spins and spin of each sublattice, respectively (see Methods). Our model predicts a redshift of the q-FM mode and a blueshift of the q-AFM mode (under the approximate condition $|B_{\text{DM}}| > S\sqrt{KJ_0}$), both linearly dependent on the laser-driven magnon population. These predictions are confirmed by the observations reported in Fig. 3**(b)** and Extended Data Fig. 4. Strikingly, our model predicts that in a collinear antiferromagnet (i.e. $|B_{\text{DM}}| = 0$) both eigenfrequencies redshift, analogously to the case of a ferromagnet².

Our experimental results show that resonantly driving the 2M Mode discloses a regime of coherent spin dynamics beyond canonical spin-wave theory, in which effectively the spin Hamiltonian of the medium is renormalised. The understanding of the microscopic processes underlying both the 2MRRS mechanism and the modification of the eigenfrequencies is still in its infancy, as the dynamics of the magnetic interactions and possible magnon-magnon interactions^{2,38} have been neglected. Nevertheless, we expect the same mechanism to be applicable to all magnetic and even magnetoelectric materials that show infrared absorption related to the 2M-process^{24,39,40}.

Methods

Sample and characterization. At room temperature hematite $\alpha\text{-Fe}_2\text{O}_3$ is a canted antiferromagnet, comprising two Fe^{3+} sublattices coupled in an antiparallel fashion by the exchange interaction (\mathbf{S}^{\uparrow} and \mathbf{S}^{\downarrow} in Fig. 1**(a)**). The DMI effectively cants the spins, inducing a net magnetization in the ab -plane ($\mathbf{M} = 5 \times 10^{-4}$ emu in Fig. 1**(a)**). For our experiments we employed a 30- μm thick single-crystal, cut along the [001] axis. The crystal was commercially purchased and polished down to the aforementioned thickness, which matches the penetration depth of light in correspondence of the 2M Mode (45 THz). We measured the absorption spectrum of $\alpha\text{-Fe}_2\text{O}_3$ shown in Fig. 1**(b)** with a commercial FTIR spectrometer. The peak value of the absorption coefficient in correspondence of the 2M Mode is 155 cm^{-1} , which was estimated taking into account also the reflectivity of $\alpha\text{-Fe}_2\text{O}_3$. A magnetic characterisation was also performed, as the hysteresis loop of the magnetization as a function of an

applied magnetic field was measured at 300 K with a superconducting quantum interference device (SQUID). The data (Extended Data Fig. 6) demonstrate that the 200 mT field applied during our pump-probe experiments is intense enough to saturate the magnetisation.

Two-magnon excitation via absorption. The early observations of the 2M Mode in the absorption spectrum of magnetic materials demonstrated this process to be of electric-dipole origin^{24,25}. Following the original and canonical treatment of the problem³⁻⁵, let us introduce the light-matter interaction as

$$H_{2M} = -\mathbf{p}_{\text{eff}} \cdot \mathbf{E}, \quad (6)$$

where \mathbf{p}_{eff} is the effective electric dipole moment and \mathbf{E} represents the electric field component of light. Taking the conservation of spin into account, the lowest-order contribution to the electric dipole moment is given by

$$\mathbf{p}_{\text{eff}} = \Pi_{ij} (\mathbf{S}_i \cdot \mathbf{S}_j), \quad (7)$$

where i, j indicate ionic sites in the crystal, the form of the tensor Π_{ij} is obtained from consideration of the crystal symmetry, $\mathbf{S}_{i,j}$ are spins located at the corresponding ionic sites. Considering nearest neighbour spins in multisublattice materials, it follows that \mathbf{S}_i and \mathbf{S}_j belong to two different sublattices. This latter consideration in combination with the form of Eq. (7) reveals why the microscopy of Π_{ij} is related to the exchange interaction³⁻⁵. Considering the pair of ions i and j belonging to two different sublattices (\uparrow and \downarrow), where a spin-up and a spin-down electrons are accommodated in the orbitals φ_i and φ_j , respectively. Formally, we can now express the transition electric dipole moment accompanying the flip of both spins as

$$\begin{aligned} \langle \varphi_{i\uparrow} \varphi_{j\downarrow} | \mathbf{P}_{\text{eff}} | \varphi_{j\uparrow} \varphi_{i\downarrow} \rangle &= \sum_{\mu} \langle \varphi_{i\uparrow} \varphi_{j\downarrow} | \mathbf{P} | \varphi_{\mu\uparrow} \varphi_{j\downarrow} \rangle \langle \varphi_{\mu\uparrow} \varphi_{j\downarrow} | V | \varphi_{j\uparrow} \varphi_{i\downarrow} \rangle / \Delta E(\varphi_{\mu} \leftarrow \varphi_i) + \\ &+ \sum_{\nu} \langle \varphi_{i\uparrow} \varphi_{j\downarrow} | \mathbf{P} | \varphi_{i\uparrow} \varphi_{\nu\downarrow} \rangle \langle \varphi_{i\uparrow} \varphi_{\nu\downarrow} | V | \varphi_{j\uparrow} \varphi_{i\downarrow} \rangle / \Delta E(\varphi_{\nu} \leftarrow \varphi_j), \end{aligned} \quad (8)$$

where \mathbf{P} is the electric-dipole moment operator, $\Delta E(\varphi_{\mu,\nu} \leftarrow \varphi_i, j)$ is the energy required for transferring an electron from $\varphi_{i,j}$ to $\varphi_{\mu,\nu}$, where $\varphi_{\mu,\nu}$ are any odd-parity orbitals in the excited state of the ion i and j , so that an allowed electric-dipole transition can occur. In the most general case ($\varphi_{\mu} \neq \varphi_j, \varphi_{\nu} \neq \varphi_i$) the interaction operator V is the two-electron Coulomb operator r_{12}^{-1} . Consequently, the matrix elements of V are the canonical exchange integrals, more specifically

$$\langle \varphi_{\mu\uparrow} \varphi_{j\downarrow} | V | \varphi_{j\uparrow} \varphi_{i\downarrow} \rangle = \int dr_1 dr_2 \varphi_{\mu}^*(\mathbf{r}_1) \varphi_j^*(\mathbf{r}_2) V \varphi_j(\mathbf{r}_1) \varphi_{\mu}(\mathbf{r}_2). \quad (9)$$

Figure 1(c) graphically displays this process. The states labelled as 1 and 2 represent $\varphi_{i,j}^{\uparrow,\downarrow}$: considering the spin orientation determined in the ground state of the system by the exchange interaction, flipping a spin while keeping the electron in the same orbital generates the ΔE_{1-2} energy split. An analogous consideration applies to the energy split of the states 3 and 4, which describe an orbital excited state. The photon energy required to induce the absorption of the magnon pair is $h\nu = 2\Delta E_{1-2}$. The blue arrow represents the spin-preserving electric dipole transition ($\langle\varphi_{i\uparrow}\varphi_{j\downarrow}|\mathbf{P}|\varphi_{\mu\uparrow}\varphi_{j\downarrow}\rangle$ in Eq. (8)), while the red arrows depict the transitions driven by the potential V . Importantly: the spin-preserving transition can be either a real electric dipole transition between two orbitals of the magnetic ions or the charge-transfer transition, depending on the electronic structure of the material under investigation.

Laser system and set-up. Our self-developed and build table-top laser system combines femtosecond Er:Fiber and Yb:Fiber technology with a high-power regenerative Yb:thin-disk amplifier. The proper thermal management of the amplification geometry⁴¹ allows for nearly transform-limited 615 fs pulses with central wavelength of 1030 nm and 17 mJ pulse energy at a repetition rate of 3 kHz⁴². The output of the laser system drives first a non-linear frequency conversion consisting of a white-light (WL) seed, generated in a YAG plate, and a subsequent three-stage optical parametric amplifier (OPA). Together with the remaining components of the Yb:thin disk amplifier (pump), the redshifted beam (signal) provided by the OPA generates intense multi-THz pulses (idler) in AgGaS₂ via difference-frequency mixing. The idler intensity is conveniently adjustable at 45 THz central frequency by polarisation-based intensity adjustment of the pump. The central frequency and bandwidth of the idler beam can be fine-tuned by varying the signal spectrum and the phasematching angle of the 2 mm-thick AgGaS₂ crystal. A parallel WL and OPA sequence generates the near-infrared probe beam spectrally covering a 56 THz-broad band at $1/e^2$ width. The duration of the probe pulses is 20 fs. This probe beam propagates collinearly with the multi-THz beam and both are focused in a 15 μm -thin GaSe crystal for field-resolved detection of the multi-THz output by electro-optic sampling. Calculations considering the maximum achievable fluence and detected electric-field waveform yield a peak electric field strength exceeding 300 MV/cm. All propagation paths of the mid-infrared beam are held in nitrogen atmosphere to avoid molecular absorption by e.g. water vapour. The electric field and spectrum of our mid-infrared laser pulses are shown in Extended Data Fig. 1. The ultrafast spin dynamics is detected by monitoring the changes of the ellipticity of the probe beam in a balanced detection scheme, comprising a quarter-wave plate, a Wollaston prism and two photodiodes. The same detection scheme has been employed to detect coherent low-energy magnons in $\alpha\text{-Fe}_2\text{O}_3$ ²⁸. In particular, it was demonstrated that in our configuration the magneto-optical Cotton-Mouton effect generates the detected ellipticity of the probe polarisation²⁸.

Data analysis. The pump-probe data were fitted using a function comprising the sum of two exponentially damped sinusoidal terms, as well as an exponential decay term, namely

$$f(t) = \sum_{i=1}^2 a_i \sin(2\pi\nu_i t + \phi_i) \exp\left(-\frac{t}{\tau_i}\right) + b_{\text{bk}} \exp\left(-\frac{t}{\tau_{\text{bk}}}\right) \quad (10)$$

where a_i , ν_i , ϕ_i and τ_i refer to the amplitude, frequency, phase and relaxation time of the q-FM and q-AFM modes, respectively. The third term describes the background on top of which the oscillations are superimposed. We determine τ_{bk} to be on the order of 100-150 ps throughout all dataset shown in the manuscript. The overall fit quality is excellent, as demonstrated by R-squared values ranging between 0.95 and 0.99. Furthermore, error bars are also extracted from the fitting procedure and represent the confidence bounds (95%) of the coefficients.

Modification of the interactions. The eigenfrequencies of the q-FM and q-AFM modes are given by the following equations^{27,28}

$$\omega_{\text{q-FM}} = \gamma \sqrt{H_0(H_0 + H_D)} \quad (11)$$

$$\omega_{\text{q-AFM}} = \gamma \sqrt{H_c^2 + H_D(H_0 + H_D)}, \quad (12)$$

where γ , H_0 and H_D represent the gyromagnetic ratio, the externally applied magnetic field and the effective field related to the Dzyaloshinski-Moriya interaction. The term $H_c^2 = 2H_e H_a$ is the product of the exchange (H_e) and anisotropy (H_a) effective fields. From Eq. (11), it follows that a change in the frequency of the q-FM mode can be expressed by

$$\Delta\omega_{\text{q-FM}} = \frac{\partial\omega_{\text{q-FM}}}{\partial H_D} \Delta H_D. \quad (13)$$

As the left-hand side of the equation is the experimentally measured modification of the frequency of the q-FM mode, once the derivative $\partial\omega_{\text{q-FM}}/\partial H_D$ is evaluated it is straightforward to calculate the renormalized Dzyaloshinski-Moriya interaction field. The value of γ was taken fitting the magnetic field dependence of the q-FM-frequency (Fig. 2(c)), noting that the result of our fitting procedure is quantitatively consistent with the literature²⁹. The value of $H_D = 2.2$ T was taken from the literature²⁷ and the value of the magnetic field H_0 entering Eq. (11) was set equal to the experimentally employed field (0.2 T). As a result we obtain $\Delta H_D = -205$ mT, which gives $\Delta H_D/H_D \approx -9\%$.

In a similar way, taking Eq. (12) as starting point, we evaluated ΔH_c^2 , using the same input values as described above, with the addition of our estimation of ΔH_D here described and $H_c^2 = 31$ T² from the literature²⁷. Following this approach we obtained $\Delta H_c^2 = 3.96$ T², which corresponds to $\Delta H_c^2/H_c^2 \approx 12\%$. We notice that while the

contributions of the anisotropy and exchange to the latter term cannot unambiguously and rigorously be disentangled, the lion share of ΔH_c^2 is expected to be attributable to the exchange interaction, given that only the spin-conserving ($\Delta S = 0$) exchange mechanism allowing to resonantly drive the 2M mode.

Theoretical basis for the excitation mechanism. We propose a mechanism based on the resonant enhancement of the efficiency of Raman scattering by the quasi-antiferromagnetic (q-AFM) and quasi-ferromagnetic (q-FM) modes, mediated by the two-magnon (2M)-excitation. In the following, we will recall the theoretical formalism for impulsive stimulated Raman scattering and then develop in analogy a formalism for the resonant enhancement by the 2M Mode, which we call two-magnon resonant Raman scattering (2MRRS).

Conventional impulsive stimulated Raman scattering (ISRS)

The fundamental Raman-type light-matter interaction mechanism of magnon modes with ultrashort laser pulses is impulsive stimulated Raman scattering (ISRS)^{9,36,43,44}. The interaction Hamiltonian is given by the coupling of the electric dipole moment, \mathbf{p} , with the electric field component of light, \mathbf{E} ,

$$H_{\text{int}} = -\mathbf{p} \cdot \mathbf{E}. \quad (14)$$

The first-order electric dipole moment for Raman scattering is given by

$$p_i = \frac{\varepsilon_0}{V} \chi_{ij} E_j. \quad (15)$$

Here, ε_0 is the vacuum permeability, V is the volume of the unit cell and χ_{ij} is the linear electric susceptibility. We use the Einstein sum convention in the following. Phenomenologically, the electric dipole moment produced by magnon modes can be written as an expansion of the electric susceptibility in terms of the components of the magnetization and antiferromagnetic vectors, \mathbf{M} and \mathbf{L} . For an antiferromagnet with two sublattices, where $\mathbf{M} = \mathbf{S}^\uparrow + \mathbf{S}^\downarrow$ and $\mathbf{L} = \mathbf{S}^\uparrow - \mathbf{S}^\downarrow$, the expansion takes the general form^{45,46}

$$\begin{aligned} \chi_{ij} = & \chi_{ij}^0 + \alpha_{ijk} M_k + \beta_{ijkl} M_k M_l + \\ & \beta'_{ijkl} M_k L_l + \beta''_{ijkl} L_k L_l + \dots \end{aligned} \quad (16)$$

The mechanism corresponding to terms linear in M_i is called the inverse Faraday effect, whereas that corresponding to quadratic terms is called the inverse Cotton-Mouton effect^{45,47}. A typical scattering and energy diagram can be found in Extended Data Figs. 7(a) and (b). The coherent spin dynamics can be captured by the Landau-Lifshitz-Gilbert equations^{11,48},

$$\frac{d\mathbf{S}_s}{dt} = -\frac{\gamma_{el}}{1+\kappa_{el}^2} \left[\mathbf{S}_s \times \mathbf{B}_s^{\text{eff}} - \frac{\kappa_{el}}{|\mathbf{S}_s|} \mathbf{S}_s \times (\mathbf{S}_s \times \mathbf{B}_s^{\text{eff}}) \right], \quad (17)$$

where \mathbf{B}^{eff} is the effective magnetic field acting on the spins, given by $\mathbf{B}_s^{\text{eff}} = -\partial H / (\partial \mathbf{S}_s)$, where $H = H_0 + H_{\text{int}}$ is the total spin Hamiltonian, containing both the ground-state Hamiltonian, H_0 , and the interaction Hamiltonian, H_{int} . The electronic gyromagnetic ratio is indicated by γ_{el} , κ_{el} is the phenomenological Gilbert damping, and the length of the spins is normalized to $|\mathbf{S}_s| = 1$.

Two-magnon resonant Raman scattering (2MRRS)

We now describe a mechanism, by which the Raman-scattering efficiency is enhanced through the two-magnon resonance. A photon is absorbed by the 2M excitation, which then scatters by the q-AFM or q-FM mode, and re-emits a photon with modified frequency. The scattering and energy diagrams of the process are shown in Extended Data Figs. 7(c) and (d).

For 2M excitations, the macrospin approximation for the magnetization and antiferromagnetic vectors is not sufficient however^{2,10,35}. The excitation is instead described by a spin-correlation function, $C_{ij,\mathbf{k}} \sim \langle S_{i,\mathbf{k}} S_{j,-\mathbf{k}} \rangle$, where $\mathbf{k} = \pi/a$ in our case of hematite. Because the electric dipole moment of the 2M excitation is given by $p_{i,\mathbf{k}} = \Pi_{ijk,\mathbf{k}} S_{j,\mathbf{k}} S_{k,-\mathbf{k}}$ ⁴, we can write the interaction potential for the absorption process as

$$H_{\text{int}} = \Pi_{ijk,\pm\mathbf{k}} C_{ij,\pm\mathbf{k}} E_{\mathbf{k}}. \quad (18)$$

The resonantly driven 2M excitation then couples nonlinearly to the q-AFM and q-FM magnons, which we again can express in terms of the macrospin approximation,

$$H_{\text{nonlinear}} = \kappa_{ijk,\pm\mathbf{k}} C_{ij,\pm\mathbf{k}}^2 M_{\mathbf{k}} + \kappa'_{ijkl,\pm\mathbf{k}} C_{ij,\pm\mathbf{k}}^2 L_{\mathbf{k}} L_{\mathbf{l}}. \quad (19)$$

Equation (19) follows the phenomenology of impulsive stimulated Raman scattering in Eq. (16). The macroscopic mechanisms can therefore be considered inverse Faraday^{6,8} and inverse Cotton-Mouton^{9,36} effects resonantly enhanced by the 2M excitation, consistent with the experimental findings. The vector of the spin correlation, \mathbf{C} , oscillates with a frequency of the 2M excitation, $C(t) \sim \sin(\omega_{2M} t)$, where $\omega_{2M} = 2\omega_{\pm\pi/a}$. That means the square of \mathbf{C} oscillates with sum- and difference-frequency components that are provided by its own linewidth, $C^2(t) \sim \sin((\omega_{2M} - \omega'_{2M}) t) + \sin((\omega_{2M} + \omega'_{2M}) t)$. The frequencies of the q-AFM and q-FM magnons at the Gamma point fall within the linewidth of the difference-frequency component generated by the square of the 2M excitation. This mechanism effectively describes a Raman scattering process, where the Raman scattering efficiency is determined

by two factors: 1) the dipole-interaction tensor of the 2M excitation, Π , and 2) the nonlinear 2M-2M-q-AFM/q-FM coupling tensors, κ and κ' . This nonlinear coupling leads to a 2M-mediated contribution to the third-order nonlinear electric susceptibility $\chi^{(3)}$. We show a schematic of the excitation pathway in Fig. 5.

The dynamics of the 2M spin-correlation function is given by the Heisenberg equation of motion³⁵

$$\hbar \frac{\partial \mathbf{C}}{\partial t} + \mathbf{C} \times \frac{\partial H}{\partial \mathbf{C}} = 0, \quad (20)$$

whereas the macrospin dynamics of the q-AFM and q-FM magnons are again described by the Landau-Lifshitz-Gilbert equations, Eq. (17). The total spin Hamiltonian is expressed as $H = H_0 + H_{\text{int}} + H_{\text{nonlinear}}$, and the spin-correlation function drives the Landau-Lifshitz-Gilbert equations as an effective magnetic field

$\mathbf{B}_s^{\text{eff}} = -\partial H_{\text{nonlinear}} / (\partial \mathbf{S}_s)$. This type of coupling process is different from the three-magnon coupling mechanism observed recently^{33,34}, which is based on magnetic dipole coupling. We further note that a coherent excitation of the 2M-state has recently been achieved through Raman scattering instead of absorption of light^{10,35}. This would make the nonlinear coupling to the q-AFM and q-FM magnons in Eq. (3) an effective four-photon process however, which we expect to be much weaker than the Raman-scattering process described here. The 2M-enhanced inverse Faraday and inverse Cotton-Mouton effects can be seen in the same light as the phonon inverse Faraday and phonon inverse Cotton-Mouton effects described recently^{47,49,50}, where optical phonons, instead of a 2M excitation act as a resonant transducer.

Theory for renormalisation of the spin Hamiltonian. We sketch here the principal aspects underlying our approach to the renormalisation of the q-FM and q-AFM frequencies. The entire derivation can be found in the Supplementary Material.

We consider a model system which describes a magnet with two sublattices characterised by the Hamiltonian

$$\hat{H} = \sum_{i,j} J_{ij} \hat{S}_i \cdot \hat{S}_j + K \sum_i \hat{S}_{i,z}^2 - B_{\text{DM}} \sum_i \hat{S}_{i,x}. \quad (21)$$

The Heisenberg exchange is antiferromagnetic and only applies to nearest neighbours ($J_{ij} = J > 0$). The anisotropy is chosen such that it's larger than zero ($K > 0$) and the spins form an antiferromagnetic configuration in the x - y plane of $\alpha\text{-Fe}_2\text{O}_3$. \hat{S}_i is the spin operator that describes the spin at the lattice site \vec{r}_i with a spin length of S . We assume $\hbar = 1$.

In the absence of an internal field ($B_{\text{DM}} = 0$) any collinear antiferromagnetic configuration of spins in the ab plane (x - y coordinates) is equally favourable. If the field is smaller than the critical field strength ($0 < B_{\text{DM}} \leq B_{\text{DMcrit}} = 2SJ_0$, with $\sum_i J_{ij} = \sum_j J_{ij} = J_0$), the spins tilt away from the y -axis along the x -axis, forming a field-

polarised state along the x -axis when the field strength is larger or equal to B_{DMcrit} . Our focus will be on $0 < B_{\text{DM}} \leq B_{\text{DMcrit}}$. The spin operators can be expressed in terms of bosonic creation and annihilation operators in the Holstein-Primakoff transformation

$$\hat{S}_{i,+} = \sqrt{2S}f(\hat{n}_i^A)\hat{a}_i, \quad \hat{S}_{i,-} = \sqrt{2S}\hat{a}_i^\dagger f(\hat{n}_i^A), \quad \hat{S}_{i,3} = S - \hat{a}_i^\dagger \hat{a}_i, \quad i \in A, \quad (22)$$

$$\hat{S}_{i,+} = \sqrt{2S}f(\hat{n}_i^B)\hat{b}_i, \quad \hat{S}_{i,-} = \sqrt{2S}\hat{b}_i^\dagger f(\hat{n}_i^B), \quad \hat{S}_{i,3} = S - \hat{b}_i^\dagger \hat{b}_i, \quad i \in B, \quad (23)$$

with $\hat{n}_i^A = \hat{a}_i^\dagger \hat{a}_i$, $\hat{n}_i^B = \hat{b}_i^\dagger \hat{b}_i$, where \hat{a}_i (\hat{b}_i) represents the annihilation (creation) operator for spin deviations on the ionic site i belonging to the sublattice A . The operator \hat{b}_i (\hat{a}_i) carries the same meaning for the other sublattice (B). Moreover the function $f(\hat{n}) = \sqrt{1 - \hat{n}/(2S)}$ in terms of the number operator \hat{n} has to be interpreted in terms of its Taylor series

$$f(\hat{n}) = 1 - \frac{\hat{n}}{4S} - \frac{\hat{n}^2}{32S^2} - \dots \quad (24)$$

Depending on the number of magnons \hat{n} compared to the spin length S the series can be terminated for lower or higher orders of \hat{n} . The lowest order $f(\hat{n}) \approx 1$ results in the linear spin wave theory. If the occupation number increases, like in the case of thermally or optically excited magnons, we get higher-order corrections. We are especially interested in the first-order correction.

$$f_1(\hat{n}) = -\frac{\hat{n}}{4S}. \quad (25)$$

Using this formalism the energy dispersion of the eigenmodes of the canted antiferromagnet in linear spin-wave theory can be calculated in terms of the conventional magnon operators $\hat{\alpha}_{\vec{k}}$ and $\hat{\beta}_{\vec{k}}$, introduced via the Bogoliubov transformation (see Supplementary Material).

First-order correction

We consider here corrections only to the exchange terms of the Hamiltonian due to population effects exclusively. The contribution of magnon-magnon scattering and possible light-induced modifications of the interactions are not treated. To investigate the effect of a larger number of magnons in the system we will consider the correction Eq. (25) to the spin ladder operators

$$\hat{S}_{i,+} = \sqrt{2S} \left(1 - \frac{\hat{n}_i^A}{4S} \right) \hat{a}_i, \quad \hat{S}_{i,-} = \sqrt{2S} \hat{a}_i^\dagger \left(1 - \frac{\hat{n}_i^A}{4S} \right), \quad i \in A, \quad (26)$$

$$\hat{S}_{i,+} = \sqrt{2S} \left(1 - \frac{\hat{n}_i^B}{4S} \right) \hat{b}_i, \quad \hat{S}_{i,-} = \sqrt{2S} \hat{b}_i^\dagger \left(1 - \frac{\hat{n}_i^B}{4S} \right), \quad i \in B. \quad (27)$$

This changes the scalar product of two spins in terms of bosonic operators as it appears in the Heisenberg exchange interaction. Out of all terms of the scalar product, we are solely interested in the fourth-order correction (see Supplementary Material).

Using the periodicity of our system, we can apply the Fourier transform to the creation and annihilation operators. In this way we can re-write all contributions to the fourth order correction of the Heisenberg Hamiltonian in the k -space (see Supplementary Material). The next step is a mean-field approximation to each pair of bosonic operators. We will regard only terms that conserve the momentum as those will dominate. Proceeding in this way (see Supplementary Material), it is possible to obtain correction terms to the energy eigenvalues which are function of the expectation values of the number operator for magnons. The correction in the energy of the magnons implies a shift of the frequency and depends on the number of magnons in the system. We want to investigate if the number of magnons excited in the system (n) increases or decreases the energy compared to the case with no magnons present. Therefore, we regard

$$\Delta \varepsilon_{\vec{k},\alpha/\beta}(n) - \Delta \varepsilon_{\vec{k},\alpha/\beta}(0). \quad (28)$$

To get a glimpse of the effect of magnons excited at the edge of the Brillouin zone on the energy of the zone-centre magnons, we will limit our analysis to a one-dimensional magnetic system. Assuming furthermore only a photoinduced magnonic population at the zone-edges, i.e. $n_{\frac{\pi}{2}}$, it is possible to derive the following final result for the energy of the two magnon modes at the center of the Brillouin zone ($k = 0$)

$$\Delta \varepsilon_{0,\alpha}(n) - \Delta \varepsilon_{0,\alpha}(0) = -\frac{1}{\varepsilon_{0,\alpha}} \frac{S J_0^2}{2N} \sin^2(2\vartheta) n_{\frac{\pi}{2}} < 0, \quad (29)$$

$$\Delta \varepsilon_{0,\beta}(n) - \Delta \varepsilon_{0,\beta}(0) = \frac{1}{\varepsilon_{0,\beta}} \frac{S J_0^2}{2N} n_{\frac{\pi}{2}} \left(\sin^2(2\vartheta) + \frac{K}{J_0} \cos(2\vartheta) \right), \quad (30)$$

where N is the number of sites in each sublattice and $\varepsilon_{0,\alpha,\beta}$ is the unperturbed energy of the q-FM and q-AFM modes, respectively. The presence of zone-edge magnons results in a reduction of the energy of the q-FM mode. The effect on the energy of the q-AFM mode varies with the angle and can either result in an increase or a decrease. For small magnetic fields and an angle close to $\pi/2$ one can show

$$\Delta\varepsilon_{0,\beta}(n) - \Delta\varepsilon_{0,\beta}(0) \approx \frac{SJ_0^2}{\varepsilon_{0,\beta}} \frac{n_{\pi}}{2N} \left(\frac{|B|^2}{S^2 J_0^2} - \frac{K}{J_0} \right) = \frac{n_{\pi}}{2SN\varepsilon_{0,\beta}} (|B|^2 - S^2 K J_0), \quad (31)$$

which for magnetic fields smaller than $S\sqrt{KJ_0}$, close to the pure antiferromagnetic configuration, leads to a reduction in the energy. For magnetic fields larger than $S\sqrt{KJ_0}$, but still small compared to J_0 we obtain an increase in the energy of the q-AFM mode.

Data availability

Source data are provided with this paper. Further datasets collected for this study are available from the corresponding authors on reasonable request.

Acknowledgements

This work was supported by the Deutsche Forschungsgemeinschaft (DFG) through the SFB1432 (425217212, Project B07). D.B. acknowledges the support of the DFG program BO 5074/1-1. The authors thanks Michaela Lammel for the SQUID Characterisation of the samples. D.B. thanks Alexey Kimel, Joe Barker, Andrea Cavalleri and Steve Johnson for useful discussions. The authors thank Stephan Eggert, Christian Beschle and Alessandro Baserga for technical support.

Author Contributions

D.B. conceived and coordinated the project. A.L. designed and established the experimental method. C.S. and L.F. performed the experiments and analysed the data under the coordination of D.B. D.W. developed the model of the dynamical renormalisation of the Hamiltonian under the supervision of W.B. D.M.J. developed the model for the 2MRRS mechanism. D.B. wrote the manuscript with contributions from all other authors.

Correspondence to: davide.bossini@uni-konstanz.de

-
1. Stohr, J. & Siegmann, H. C. *Magnetism From Fundamentals to Nanoscale Dynamics* (2006).
 2. Kittel, C. *Quantum theory of solids* (Wiley, New York, 1987).
 3. Moriya, T., Tanabe, Y. & Sugano, S. Magnon-Induced Electric Dipole Transition Moment. *Physical Review Letters* **15**, 1023 – 1025 (1965). URL <http://link.aps.org/doi/10.1103/PhysRevLett.15.1023>.
 4. Moriya, T. Theory of Absorption and Scattering of Light by Magnetic Crystals. *Journal of Applied Physics* **39**, 1042 (1968). URL <http://link.aip.org/link/?JAPIAU/39/1042/1>.
 5. Loudon, R. Theory of infra-red and optical spectra of antiferromagnets. *Advances in Physics* **17**, 243 – 280 (1968). URL <http://www.tandfonline.com/doi/abs/10.1080/00018736800101296#.Va9fTXgqt0s>.
 6. Kirilyuk, A., Kimel, A. V. & Rasing, T. Ultrafast optical manipulation of magnetic order. *Reviews of Modern Physics* **82**, 2731 – 2784 (2010). URL <http://link.aps.org/doi/10.1103/RevModPhys.82.2731>.
 7. Bossini, D. & Rasing, T. Femtosecond optomagnetism in dielectric antiferromagnets. *Physica Scripta* **92**, 024002 (2017).
 8. Kimel, A. V. *et al.* Ultrafast non-thermal control of magnetization by instantaneous photomagnetic pulses. *Nature* **435**, 655 – 657 (2005). URL <http://dx.doi.org/10.1038/nature03564>.
 9. Kalashnikova, A. M. *et al.* Impulsive Generation of Coherent Magnons by Linearly Polarized Light in the Easy-Plane Antiferromagnet FeBO₃. *Physical Review Letters* **99**, 167205 (2007). URL <http://link.aps.org/doi/10.1103/PhysRevLett.99.167205>.
 10. Bossini, D. *et al.* Macrospin dynamics in antiferromagnets triggered by sub-20 femtosecond injection of nanomagnons. *Nature Communications* **7**, 10645 (2016). URL <http://www.nature.com/ncomms/2016/160205/ncomms10645/full/ncomms10645.html>.
 11. Kampfrath, T. *et al.* Coherent terahertz control of antiferromagnetic spin waves. *Nature Photonics* **5**, 31 – 34 (2010). URL <http://dx.doi.org/10.1038/nphoton.2010.259>.
 12. Makihara, T. *et al.* Ultrastrong magnon-magnon coupling dominated by antiresonant interactions. *Nature Communications* **12**, 3115 (2021).
 13. Schlauderer, S. *et al.* Temporal and spectral fingerprints of ultrafast all-coherent spin switching. *Nature* **569**, 383 – 387 (2019).

14. Stupakiewicz, A., Szerenos, K., Afanasiev, D., Kirilyuk, A. & Kimel, A. V. Ultrafast nonthermal photo-magnetic recording in a transparent medium. *Nature* **542**, 71 (2017).
15. Belvin, C. A. *et al.* Exciton-driven antiferromagnetic metal in a correlated van der Waals insulator. *Nature Communications* **12**, 4837 (2021). 2106.08355.
16. Bossini, D. *et al.* Ultrafast Amplification and Nonlinear Magnetoelastic Coupling of Coherent Magnon Modes in an Antiferromagnet. *Physical Review Letters* **127**, 077202 (2021).
17. Bossini, D. *et al.* Femtosecond activation of magnetoelectricity. *Nature Physics* **14**, 370 – 374 (2018).
18. Hashimoto, Y. *et al.* All-optical observation and reconstruction of spin wave dispersion. *Nature Communications* **8**, 15859 (2017).
19. Nova, T. F. *et al.* An effective magnetic field from optically driven-phonons. *Nature Physics* **13**, 132 – 136 (2016).
20. Afanasiev, D. *et al.* Ultrafast control of magnetic interactions via light-driven phonons. *Nature Materials* 1–5 (2021). 1912.01938.
21. Kawasaki, T. Possibility of inverse Suhl instability processes by optical pumping in antiferromagnets. *Journal of Magnetic Resonance (1969)* **9**, 114 – 117 (1973).
22. Odagaki, T. Photon Pumped Spin Wave Instability in Rutile-Type Antiferromagnets. *Journal of the Physical Society of Japan* **35**, 40–46 (1973).
23. Samuelsen, E. J. & Shirane, G. Inelastic neutron scattering investigation of spin waves and magnetic interactions in α -Fe₂O₃. *physica status solidi (b)* **42**, 241 – 256 (1970).
24. Richards, P. L. Far-Infrared Absorption by Two-Magnon Excitations in Antiferromagnets. *Journal of Applied Physics* **38**, 1500 – 1504 (2004).
25. Azuma, S. *et al.* Optical response due to many magnons in α -Fe₂O₃. *Physical Review B* **71**, 014429 (2005). URL <http://link.aps.org/doi/10.1103/PhysRevB.71.014429>.
26. Velikov, L., Mironov, S. V. & Rudashevskii, E. C. Study of the interaction between two spin oscillation modes during anti-ferromagnetic resonance in the weakly ferromagnetic phase of hematite. *Soviet Physics JETP* **30**, 428–432 (September 1969).
27. Velikov, L. & Rudashevskii, E. Antiferromagnetic resonance In hematite in the weakly ferromagnetic state. *Soviet Physics JETP* **29**, 836–839 (May 1969).
28. Grishunin, K., Mashkovich, E. A., Kimel, A. V., Balbashov, A. M. & Zvezdin, A. K. Excitation and detection of terahertz coherent spin waves in antiferromagnetic α -Fe₂O₃. *Physical Review B* **104**, 024419 (2021).

29. Lebrun, R. *et al.* Long-distance spin-transport across the Morin phase transition up to room temperature in ultra-low damping single crystals of the antiferromagnet α -Fe₂O₃. *Nature Communications* **11**, 6332 (2020). 2005.14414.
30. Chou, S. G. *et al.* High-Resolution Terahertz Optical Absorption Study of the Antiferromagnetic Resonance Transition in Hematite α -Fe₂O₃. *The Journal of Physical Chemistry C* **116**, 16161 – 16166 (2012).
31. Mashkovich, E. A. *et al.* Terahertz light-driven coupling of antiferromagnetic spins to lattice. *Science* **374**, 1608–1611 (2021). 2111.10186.
32. Lu, J. *et al.* Coherent Two-Dimensional Terahertz Magnetic Resonance Spectroscopy of Collective Spin Waves. *Physical Review Letters* **118**, 207204 (2017). URL <https://journals.aps.org/prl/abstract/10.1103/PhysRevLett.118.207204>.
33. Zhang, Z. *et al.* Nonlinear coupled magnonics: Terahertz field-driven magnon upconversion. *arXiv* (2022). 2207.07103.
34. Zhang, Z. *et al.* Three-wave mixing of anharmonically coupled magnons. *arXiv* (2023). 2301.12555.
35. Formisano, F. *et al.* Coherent thz spin dynamics in antiferromagnets beyond the macrospin approximation. *ArXiv* (2023). URL <https://arxiv.org/abs/2303.06996>. 2303.06996.
36. Kalashnikova, A. M. *et al.* Impulsive excitation of coherent magnons and phonons by subpicosecond laser pulses in the weak ferromagnet FeBO₃. *Physical Review B* **78**, 104301 (2008). URL <http://link.aps.org/doi/10.1103/PhysRevB.78.104301>.
37. Dannegger, T. *et al.* Magnetic properties of hematite revealed by an ab initio parameterized spin model. *Physical Review B* **107**, 184426 (2023). 2301.13094.
38. Schlickeiser, F. *et al.* Temperature dependence of the frequencies and effective damping parameters of ferrimagnetic resonance. *Physical Review B* **86**, 214416 (2012).
39. Kocsis, V. *et al.* Identification of Antiferromagnetic Domains Via the Optical Magnetoelectric Effect. *Phys. Rev. Lett.* **121**, 979 (2018).
40. Peedu, L. *et al.* Spin excitations of magnetoelectric LiNiPO₄ in multiple magnetic phases. *Physical Review B* **100**, 024406 (2019). 1904.06106.
41. Giesen, A. *et al.* Scalable concept for diode-pumped high-power solid-state lasers. *Applied Physics B* **58**, 365–372 (1994).
42. Fischer, J. *et al.* 615-fs pulses with 17 mJ energy generated by an Yb:thin-disk amplifier at 3 kHz repetition rate. *Optics Letters* **41**, 246 (2016).

43. Popova, D., Bringer, A. & Blügel, S. Theory of the inverse Faraday effect in view of ultrafast magnetization experiments. *Phys. Rev. B* **84**, 214421 (2011).
44. Popova, D., Bringer, A. & Blügel, S. Theoretical investigation of the inverse Faraday effect via a stimulated Raman scattering process. *Phys. Rev. B* **85**, 094419 (2012).
45. Kalashnikova, A. M., Kimel, A. V. & Pisarev, R. V. Ultrafast opto-magnetism. *Physics-Uspokhi* **58**, 969–980 (2015).
46. Tzschaschel, C. *et al.* Ultrafast optical excitation of coherent magnons in antiferromagnetic NiO. *PRB* **95**, 174407 (2017).
47. Juraschek, D. M., Narang, P. & Spaldin, N. A. Phono-magnetic analogs to opto-magnetic effects. *PRR* **2**, 043035 (2020).
48. Rezende, S. M., Azevedo, A. & Rodríguez-Suárez, R. L. Introduction to antiferromagnetic magnons. *J. Appl. Phys.* **126**, 151101 (2019).
49. Juraschek, D. M., Neuman, T. & Narang, P. Giant effective magnetic fields from optically driven chiral phonons in 4f paramagnets. *Physical Review Research* **4**, 013129 (2022). 2007.10556.
50. Luo, J. *et al.* Large effective magnetic fields from chiral phonons in rare-earth halides. *arXiv* 2306.03852 (2023).

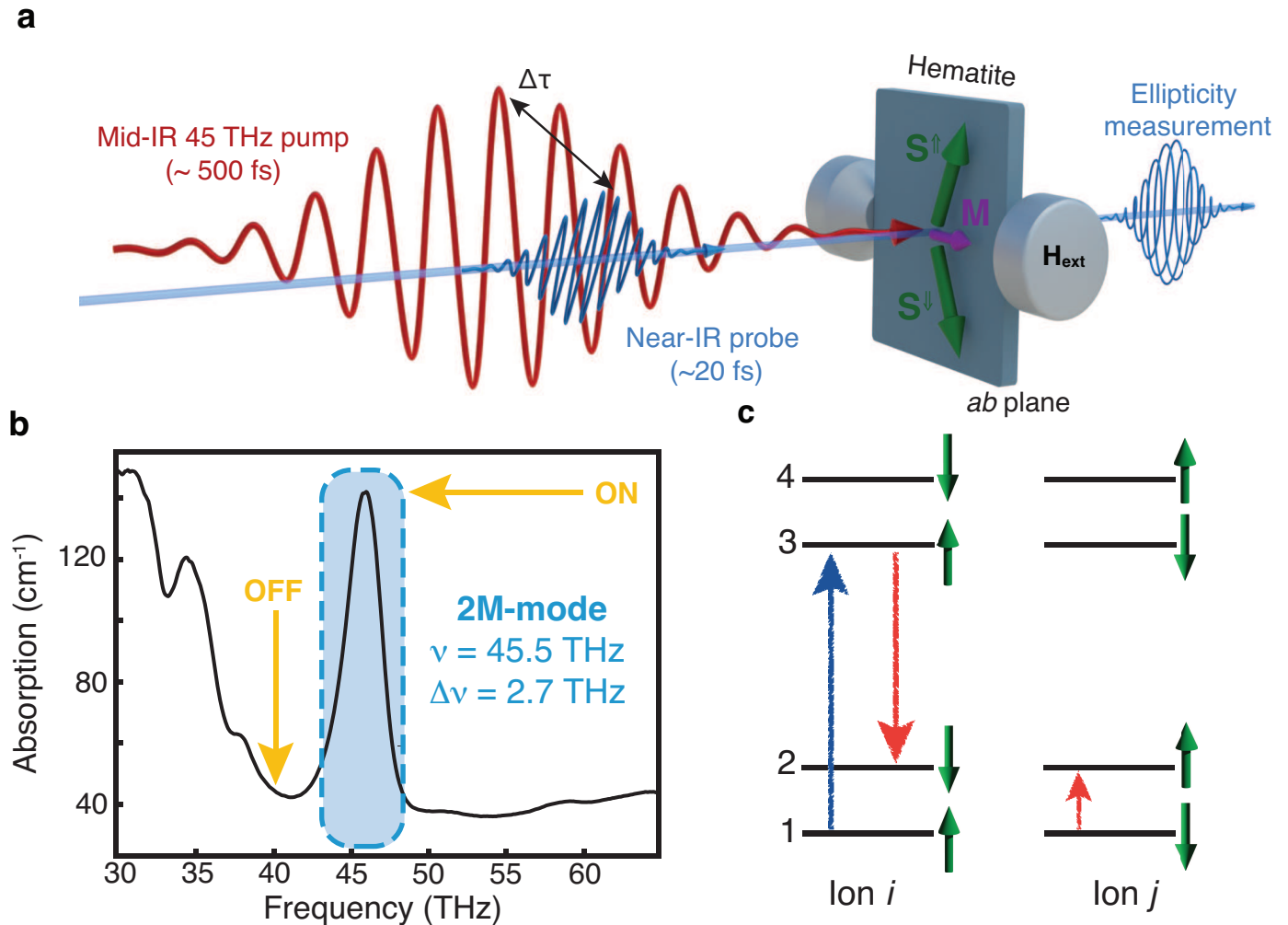


Figure 1: Concept of the experiment. **a)** Sketch of the experimental set-up. Mid-infrared pump pulses with central frequency in the 37-53 THz range trigger spin dynamics, which is detected by measuring changes of the ellipticity of the near-infrared probe beam with central wavelength of $1.2 \mu\text{m}$. A magnetic field of 200 mT is applied in the plane of the sample by means of permanent magnets to saturate the magnetisation (see Methods).

All experiments were performed at room temperature. **(b)** Room-temperature absorption spectrum of our $\alpha\text{-Fe}_2\text{O}_3$ sample in the mid-infrared spectral range measured with an FTIR spectrometer. We ascribe the peak observed at $\nu = 45 \text{ THz}$ with bandwidth $\Delta\nu = 2.7 \text{ THz}$ to the 2M Mode, fully consistently with the literature²⁵. The

conditions of resonant ("ON") and off-resonant ("OFF") pumping are indicated. **(c)** Sketch of the exchange mechanism^{3,4}. The green arrows describe the spin state of all the levels shown. The blue arrow represents a spin-preserving electric-dipole transition, while the red arrows describe exchange-driven processes (see Methods). The initial and final states differ by the energy of a magnon pair, i.e. a spin flip at each ionic site: the

2M Mode is thus optically excited.

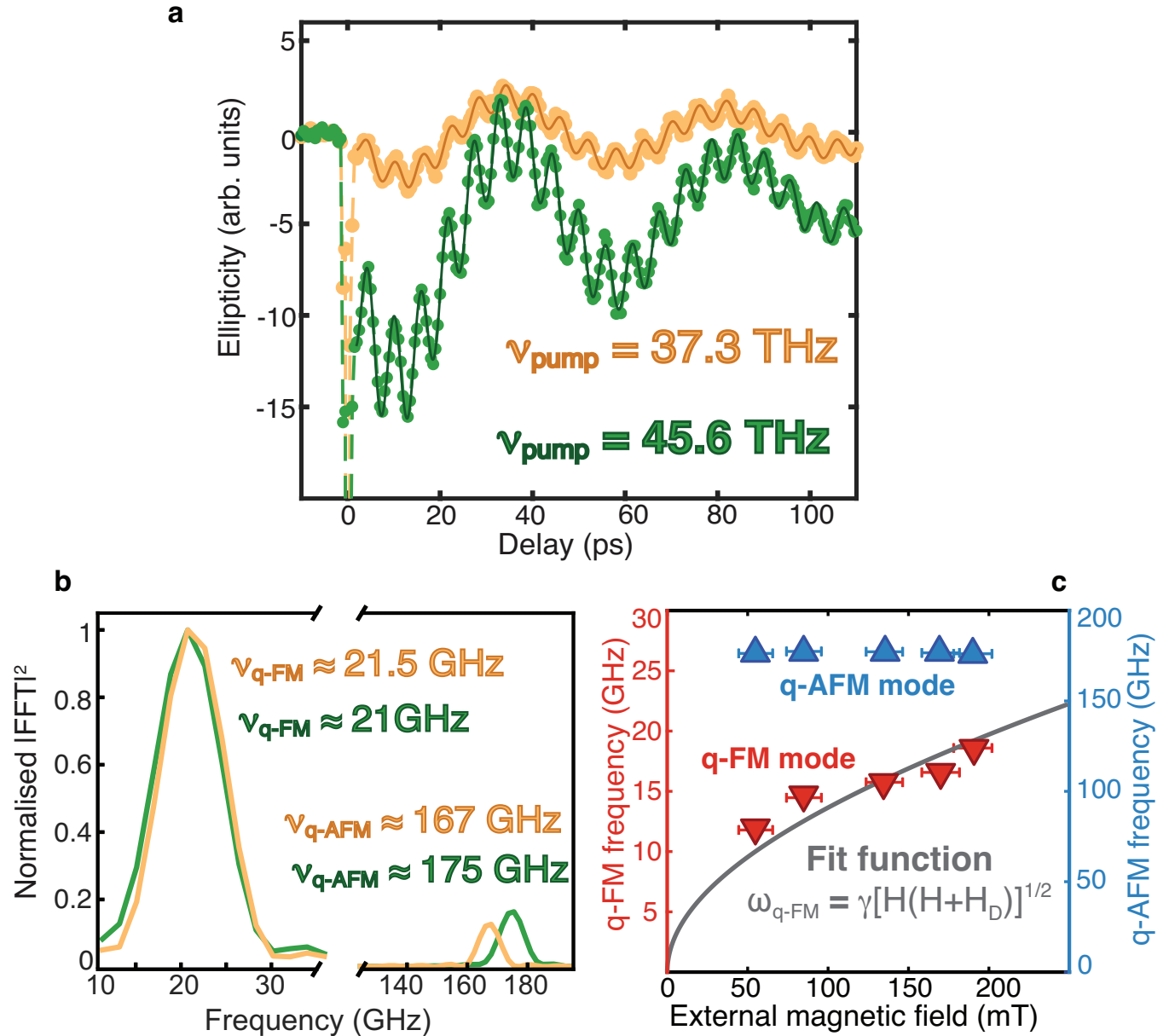


Figure 2: Optical generation of low-energy magnons. (a) The spin dynamics photoinduced by pumping the 2M mode off-resonantly (yellow line) and resonantly (green line) is plotted. Both measurements were performed exciting $\alpha\text{-Fe}_2\text{O}_3$ with pump and probe beams linearly polarised along the direction parallel and orthogonal to the magnetic field, respectively. The fluence was set to 6 mJ/cm^2 . The excitation frequency of the pump beams are shown on the figure. The continuous lines are fit to the data (see Methods). (b) Spectra of the time traces in panel (a). The square modulus of the Fourier transform of the measurements in (a) is shown. (c) Dependence of the frequencies of the q-AFM and q-FM modes on an externally applied magnetic field. The measurements were performed under the same experimental conditions of the green curve in panel (a). The field dependence of the q-FM mode was fitted with the equation shown in the figure²⁷. We obtained $\gamma = 28.5 \pm 3.5 \text{ GHz/T}$, which is quantitatively consistent with the literature²⁹.

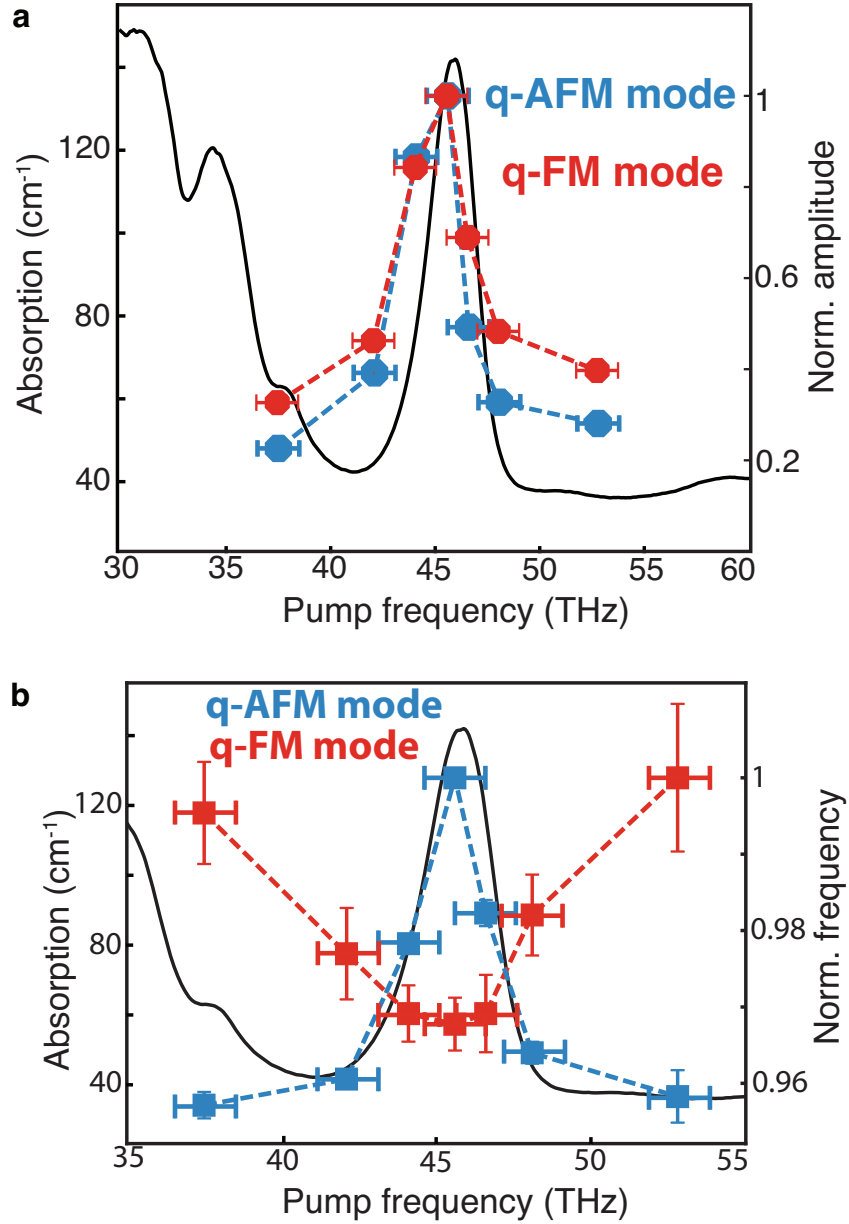


Figure 3: Photoinduced modification of the magnon spectrum. The dependence of the amplitude (a) and of the frequency (b) of the low-energy magnon modes on the pump beam frequency are shown. The data are normalised on the maximum value of each data-set. In both cases, the absorption spectrum of $\alpha\text{-Fe}_2\text{O}_3$ is plotted in the background (black line). The peak centred at 45 THz is the 2M Mode. Pump and probe beams were linearly polarised along the direction parallel and orthogonal to the magnetic field, respectively. The fluence was set to 6 mJ/cm^2 . The errorbars in the y-axis are defined as 95% confidence bounds of the fit. The error bars in the x-axis are given by the spectral bandwidth of the excitation.

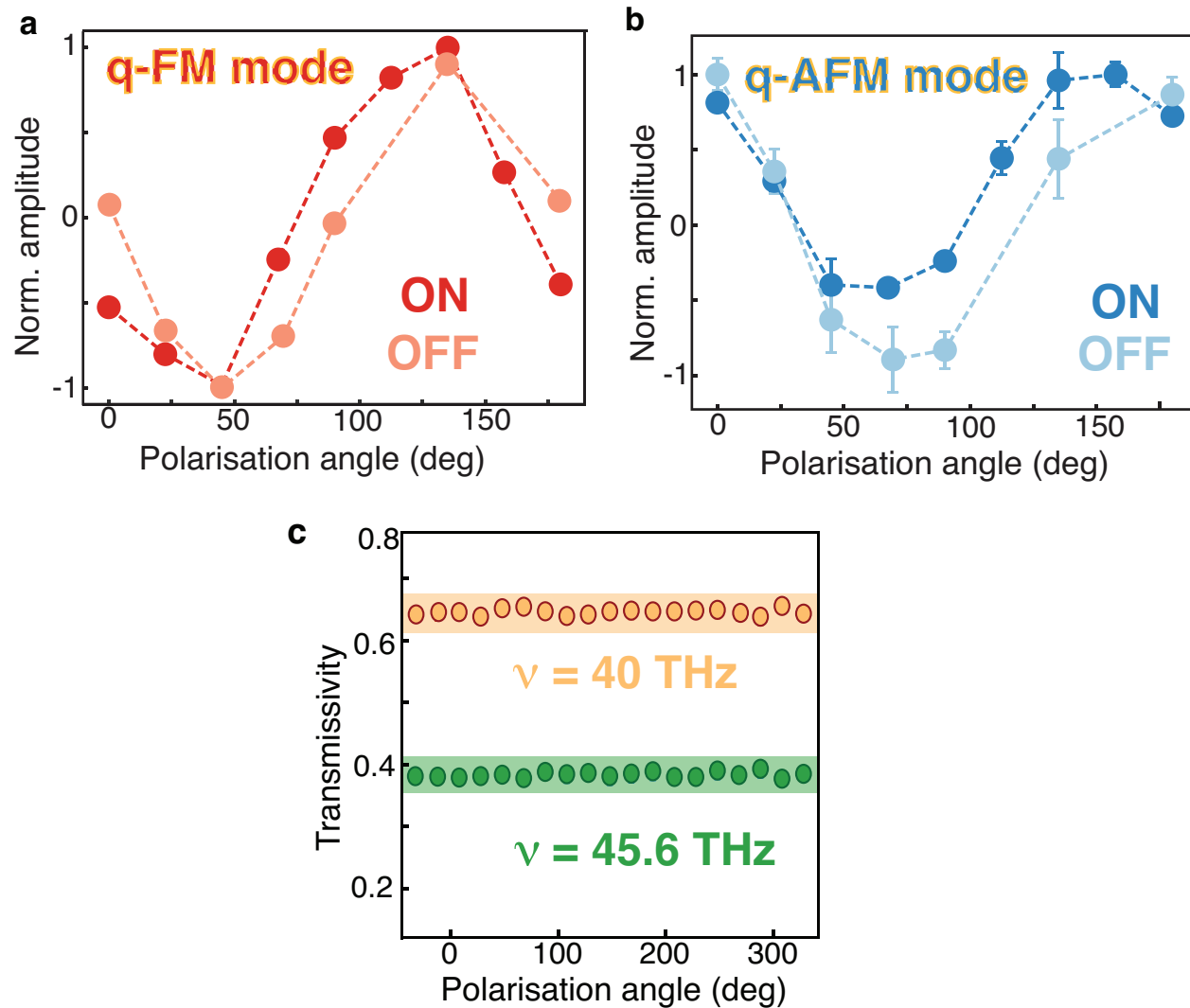


Figure 4: Pump polarisation dependence of the spin dynamics and absorption. The normalised amplitude of the q-FM (a) and q-AFM (b) mode depends 180°-periodically on the angle of linear polarisation of the pump beam. The periodicity of the dependence is not affected by the choice of the pump frequency. The probe beam was linearly polarised along the direction orthogonal to the magnetic field. The fluence was set to 6 mJ/cm². The entire data set is reported in Extended Data Fig. 3. (c) Polarisation dependence of the absorption of α -Fe₂O₃ in the ab-plane for mid-IR frequencies resonant and off-resonant with the 2M Mode. The green and yellow-shaded area corresponds to the experimental uncertainty.

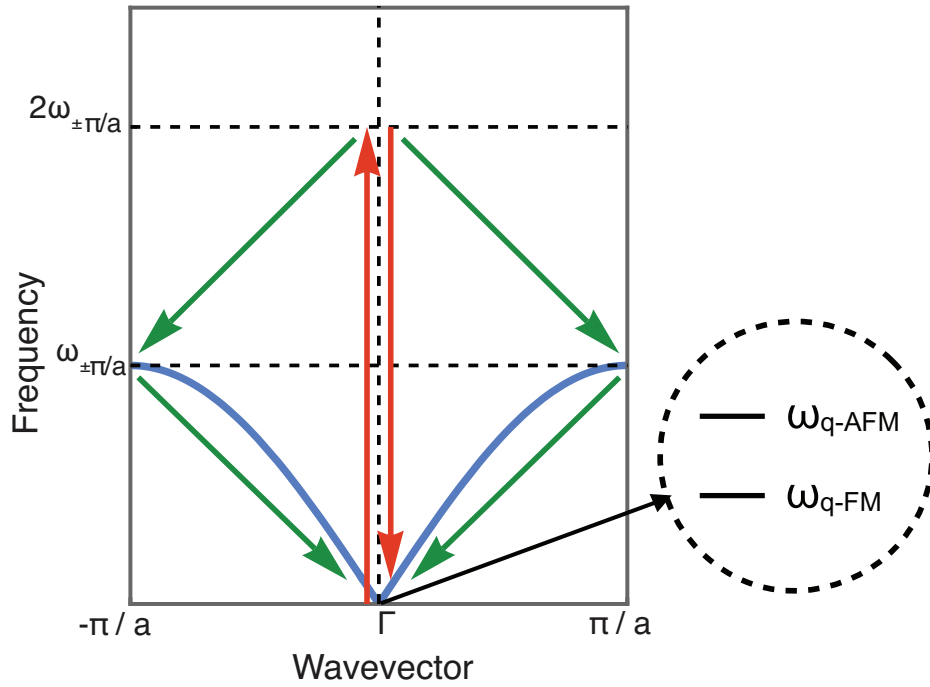
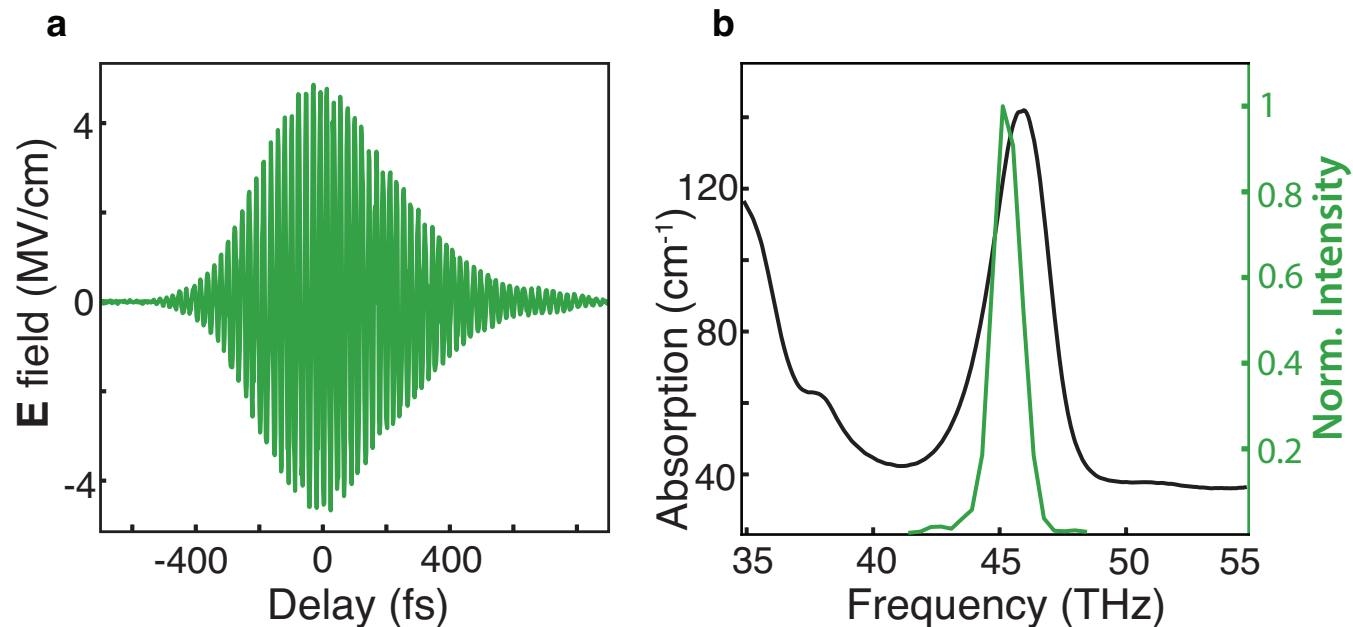
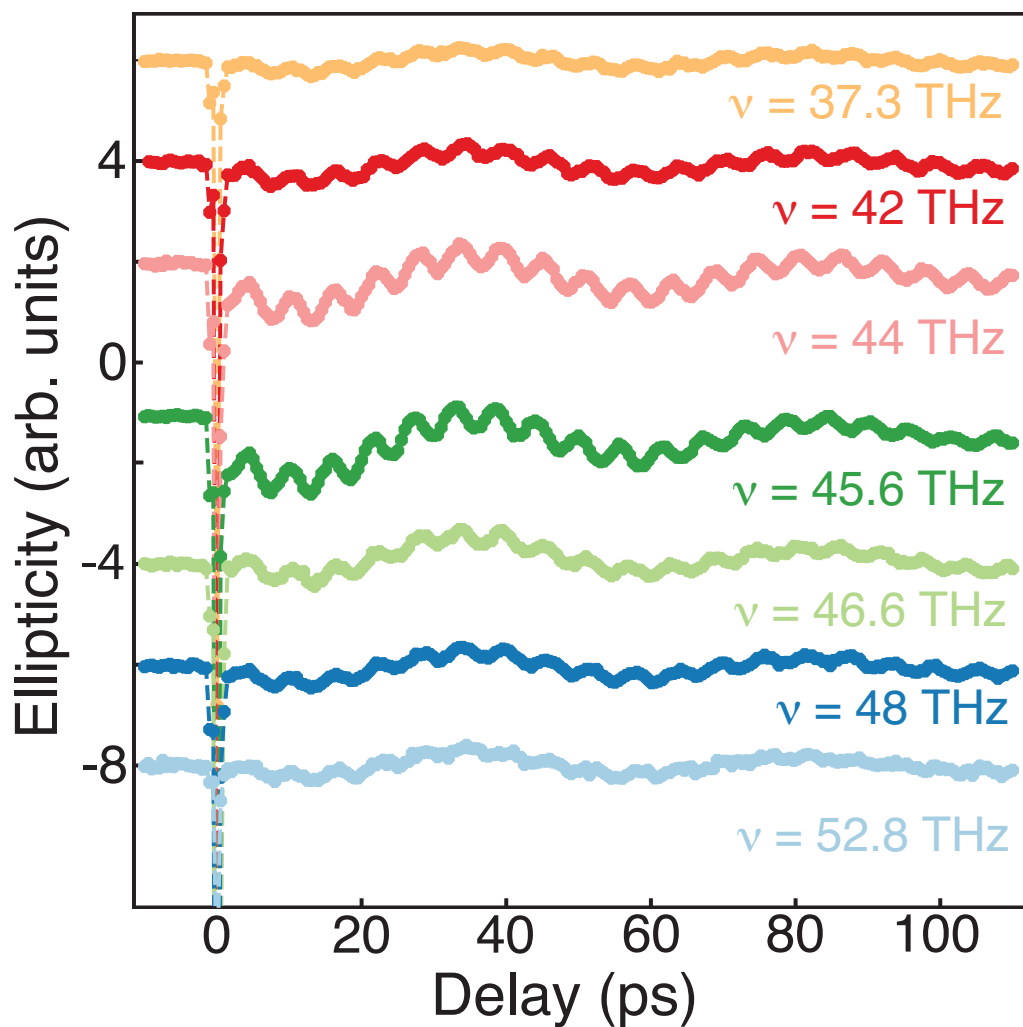


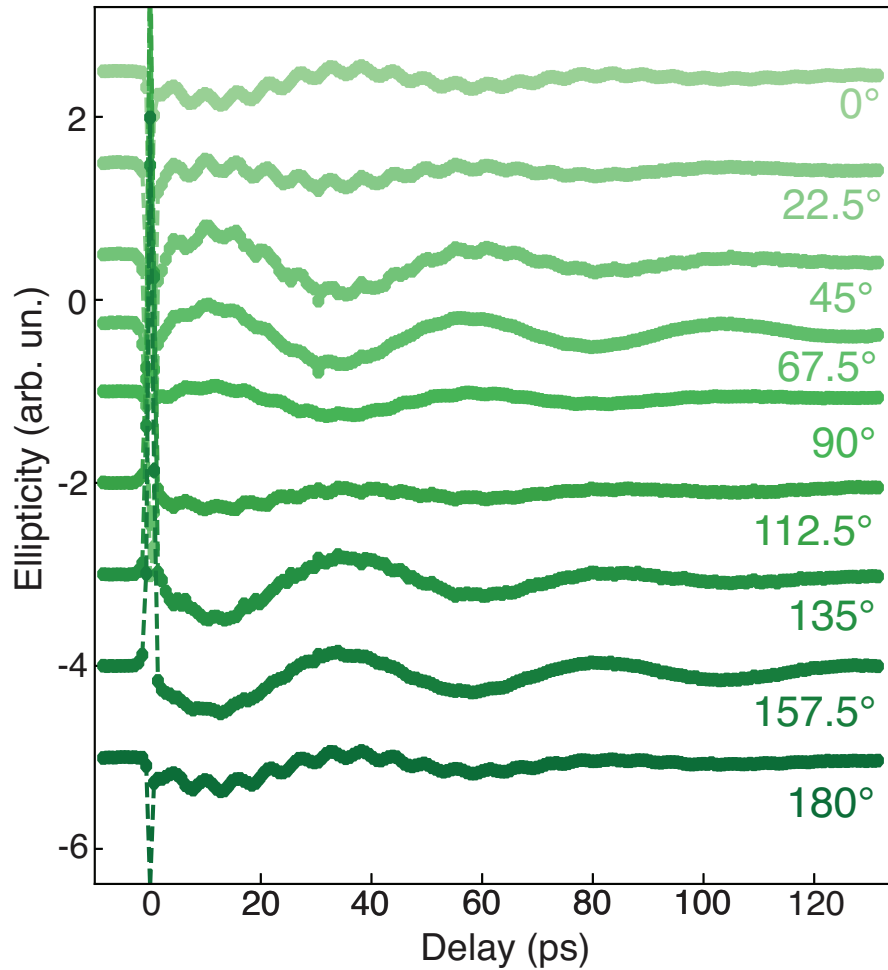
Figure 5: **Excitation mechanism.** Schematic of the spin-wave dispersion (blue curve) and two-magnon resonant Raman scattering (2MRRS). Ultrashort mid-IR pulses resonantly excite pairs of magnons near opposite edges of the Brillouin zone with frequencies $\omega_{\pm\pi/a}$ via mid-IR absorption (red up-arrow and top green arrows). Afterwards, the 2M excitation couples to the q-AFM and q-FM modes with frequencies $\omega_{q\text{-AFM}}$ and $\omega_{q\text{-FM}}$ at the centre of the Brillouin zone, under mid-IR emission (bottom green arrows and red down-arrow).



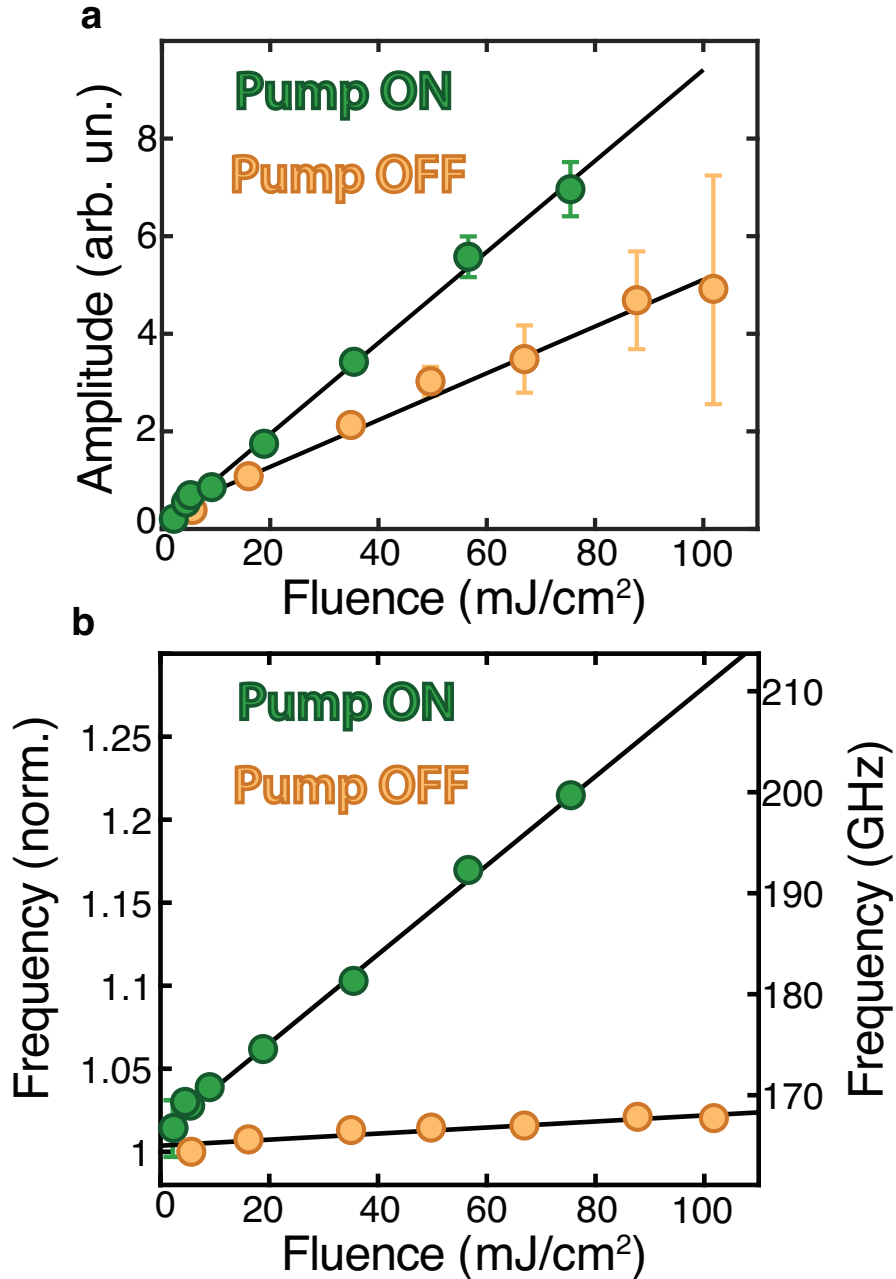
Extended Data Figure 1: **Mid-infrared laser pulses.** (a) Electric field of the femtosecond laser pulses with central frequency of 45 THz employed to measure the green time trace in Fig. 2. The field corresponds to a fluence of 6 mJ/cm². The field was measured via electro-optical sampling with the probe beam, employed also to detect the transient spin dynamics. (b) Spectrum corresponding to the electric field in panel (a), shown on top of the absorption spectrum of α -Fe₂O₃. The bandwidth of the laser pulses and of the 2M Mode are comparable.



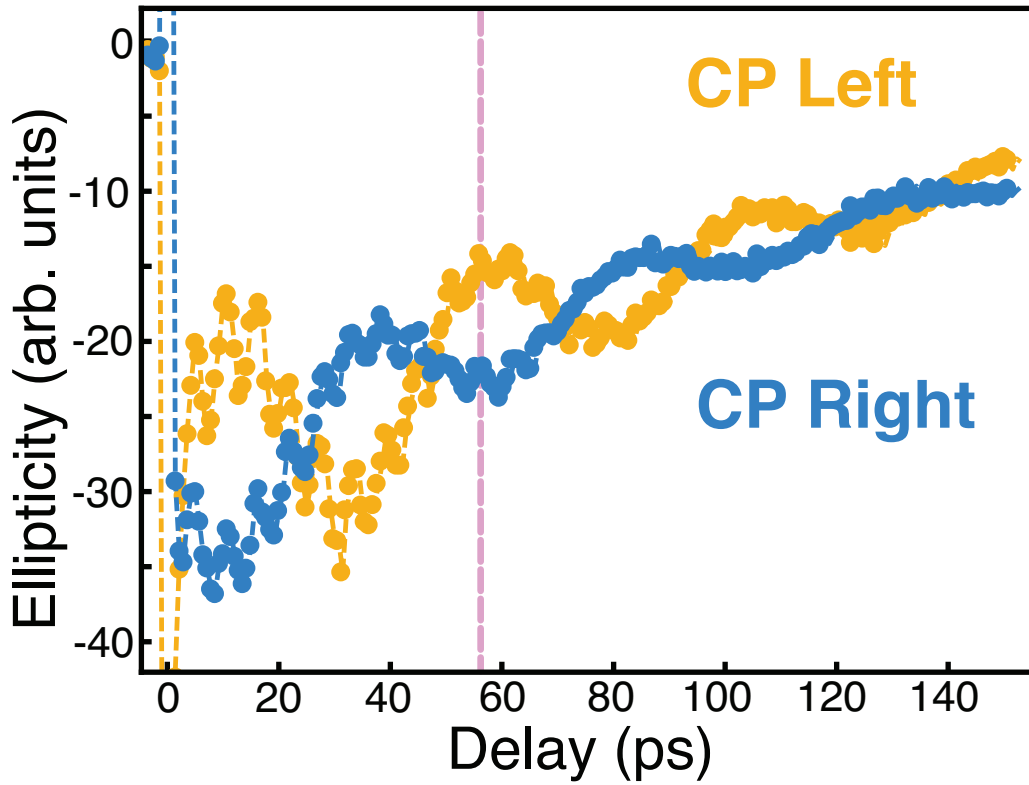
Extended Data Figure 2: **Spectral dependence of the spin dynamics.** The real-time spin dynamics as a function of the pump central frequency is shown. The pump central frequency is indicated for each data set. Pump and probe beams were linearly polarised along the direction parallel and orthogonal to the magnetic field, respectively. The fluence was set to 6 mJ/cm^2 . The transient ellipticity of the probe polarisation was monitored in the balanced-detection scheme.



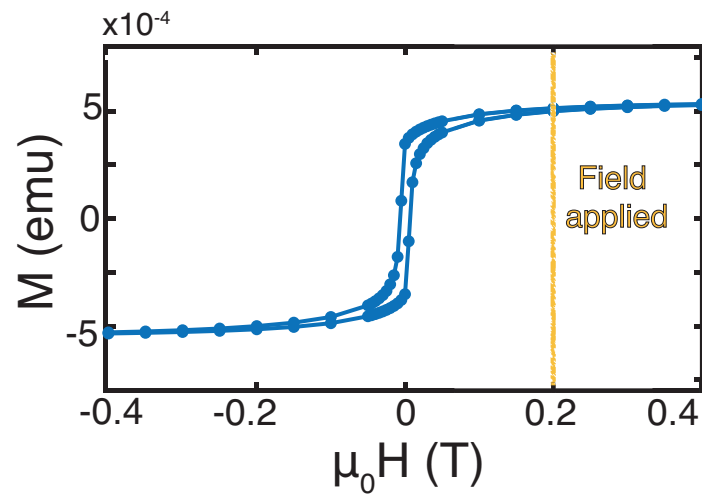
Extended Data Figure 3: **Pump polarisation dependence of the spin dynamics.** The entire dataset describing the dependence of the spin dynamics on the pump polarisation is shown. The measurements were performed under the condition of resonant excitation of the 2M Mode ("ON" in Fig. 4). The probe beam is linearly polarised along the direction orthogonal to the magnetic field. The polarisation of pump beam parallel to the external magnetic field for an angle of 0° . The fluence was set to 6 mJ/cm^2 . The transient ellipticity of the probe polarisation was monitored in the balanced-detection scheme.



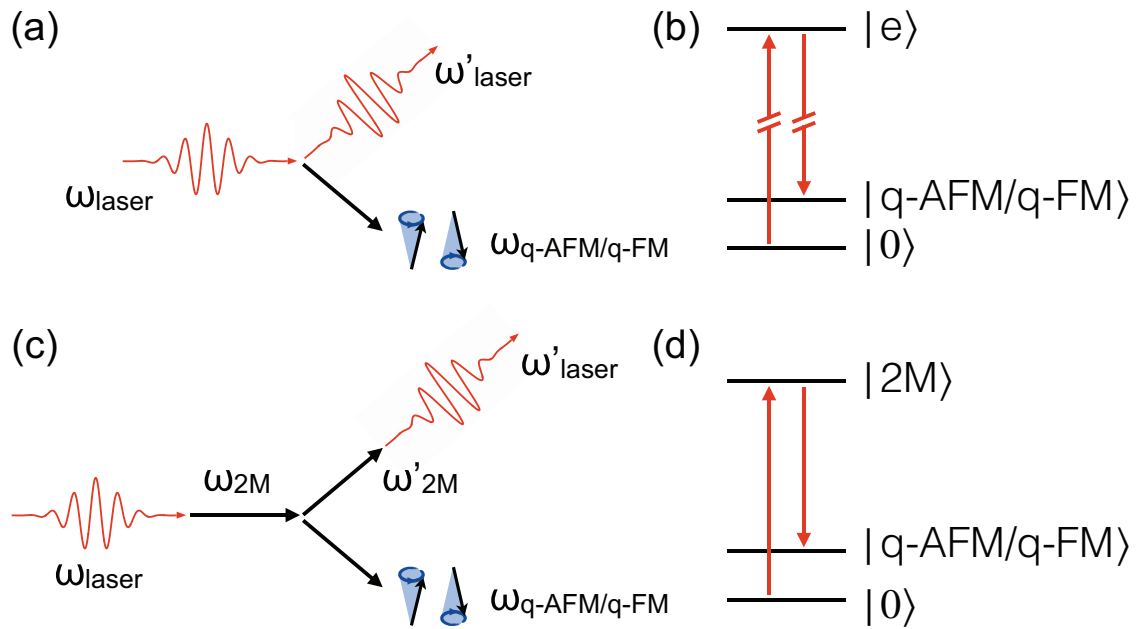
Extended Data Figure 4: **Fluence dependence of the q-AFM mode.** The dependences of the amplitude (a) and frequency (b) of the q-AFM mode on the fluence for different pump frequencies ("ON" = 45 THz, "OFF" = 39 THz) are reported. Pump and probe beams were linearly polarised along the direction parallel and orthogonal to the magnetic field, respectively. The amplitude of the q-AFM mode scales linearly (the black lines are fit to the data) with the fluence. The fluence dependence of the frequency is also linear. The modification of the frequency observed via off-resonant pumping is negligible in comparison with resonant pumping. Comparing quantitatively the slopes of the fitting curves (black lines), in the on-resonant case this value is more than 10 times bigger than in the off-resonant case. The minor modification of the frequency observed pumping far away from the resonance is ascribed to single-mode anharmonicity effects of the spin dynamics, due to the large amplitude of the spin oscillations.



Extended Data Figure 5: **Spin dynamics induced by circularly polarised mid-infrared laser pulses.** The dependence of the spin dynamics on the helicity of circularly polarised pump beams is shown. The pump central frequency was set to 45 THz, resonant to the 2M Mode. The probe beam was linearly polarised along the direction orthogonal to the magnetic field. The fluence was set to 6 mJ/cm^2 . Changing the helicity of the pump beam reverses the phase of the q-FM mode (as highlighted by the magenta dashed line), while leaving the phase of the q-AFM unaffected.



Extended Data Figure 6: **Magnetic hysteresis loop of $\alpha\text{-Fe}_2\text{O}_3$** . The measurements were performed with a SQUID at room temperature. The magnetic field was applied in the plane of the sample, similarly to our experimental geometry for the time-resolved experiments. The value of the field externally applied during the pump-probe measurements is shown. The magnetisation was saturated, which makes our experiment stroboscopic.



Extended Data Figure 7: **Impulsive stimulated Raman scattering (ISRS) vs two-magnon resonant Raman scattering (2MRRS)**. (a) In ISRS, a photon gets scattered by a magnon (here, by the q-FM or q-AFM magnon), according to the inverse Faraday or inverse Cotton-Mouton effect^{8,9}. (b) Energy diagram of ISRS, where the intermediate state is given by a virtual or real electronic state, $|e\rangle$. (c) In 2MRRS, a photon gets absorbed by the 2M excitation, which then scatters by the q-FM or q-AFM magnon and re-emits a photon with a different frequency, leading to an effective Raman scattering mechanism, resonantly enhanced by the 2M Mode. (d) Energy diagram of 2MRRS, where the intermediate state is given by the 2M excitation, $|2M\rangle$.